Global Observations of Aerosol Indirect Effects from Marine Liquid Clouds

Casey J. Wall[1], Trude Storelvmo[1,2], Anna Possner[3]

[1]Department of Geosciences, University of Oslo, Oslo, 0371, Norway
5 [2]Nord University, Bodø, 8026, Norway
[3]Institute for Atmospheric and Environmental Sciences, Goethe University Frankfurt, Frankfurt, 60438, Germany

Correspondence to: Casey J. Wall (c.j.wall@geo.uio.no)

Abstract. Interactions between aerosols and liquid clouds are one of the largest sources of uncertainty in the historical radiative forcing of climate. One widely shared goal to reduce this uncertainty is to decompose radiative anomalies arising
10 from aerosol-cloud interactions into components associated with changes in cloud-droplet number concentration (Twomey effect), liquid water path adjustments, and cloud-fraction adjustments. However, there has not been a quantitative foundation for simultaneously estimating these components with global satellite observations. Here we present a method for assessing shortwave radiative flux anomalies from the Twomey effect and cloud adjustments over ocean between 55°S and 55°N. We find that larger aerosol concentrations are associated with widespread cloud brightening from the Twomey effect, a positive
15 radiative adjustment from decreasing liquid water path in subtropical stratocumulus regions, and a negative radiative adjustment from increasing cloud fraction in the subtropics and midlatitudes. The Twomey effect and total cloud adjustment contribute -0.77 ± 0.25 W m^{-2} and -1.02 ± 0.43 W m^{-2}, respectively, to the effective radiative forcing since 1850 over the domain (95% confidence). Our findings reduce uncertainty in these components of aerosol forcing and suggest that cloud adjustments make a larger contribution to the forcing than is commonly believed.

20 **1 Introduction**

Changes in aerosol concentrations over the industrial era have modified clouds and perturbed the global radiation balance at the top of the atmosphere. The radiative flux perturbation resulting from these cloud changes, known as the effective radiative forcing from aerosol-cloud interactions (ERF$_{aci}$), is estimated to be -0.84 ± 0.61 W m^{-2} between 1750 and 2019 (90% confidence interval (CI) from Forster et al. (2021)). ERF$_{aci}$ is much more uncertain than the positive radiative
25 forcing from carbon dioxide changes ($+2.16 \pm 0.26$ W m^{-2}), meaning that ERF$_{aci}$ offsets a potentially large but highly uncertain portion of historical greenhouse-gas forcing. Reducing this uncertainty would improve assessments of climate sensitivity and committed future warming (Matthews and Zickfeld, 2012; Mauritsen and Pincus, 2017; Sherwood et al., 2020).

An extension of these forcing estimates is to characterize how changes in different cloud properties contribute to
30 ERF$_{aci}$, thereby providing insight into the relative importance of different processes. For instance, as cloud condensation

nuclei (CCN) become more abundant, liquid clouds typically form smaller but more numerous droplets. The change in cloud droplet effective radius (r_e) and number concentration (N_d) directly increases cloud optical thickness – a mechanism known as the Twomey effect (Twomey, 1977). The reduction of cloud droplet size can also enhance evaporation or reduce precipitation, causing adjustments in cloud thickness, lifetime, or morphology. Separating the radiative impacts of the Twomey effect and cloud adjustments is thus an important step towards understanding the causes of ERF$_{aci}$.

Recent community assessments find that the components of ERF$_{aci}$ all have considerable uncertainty. The Sixth Assessment Report of the Intergovernmental Panel on Climate Change (IPCC) estimates that the Twomey effect is -0.7 ± 0.5 W m^{-2}, the adjustment of liquid water path (LWP) is $+0.2 \pm 0.2$ W m^{-2}, and the adjustment of liquid-cloud fraction is -0.5 ± 0.4 W m^{-2} (90% CIs for forcing between 1750 and 2014) (Forster et al., 2021). Another assessment by the World Climate Research Programme reports even larger uncertainties (Bellouin et al., 2020). In particular, they find that the cloud-fraction adjustment is especially uncertain: It could be negligibly small or large enough to offset most of the historical carbon-dioxide forcing.

Constraints from satellite observations offer a path toward reducing this uncertainty, but in practice it has been difficult to isolate relationships between aerosols and radiative anomalies caused by changes in individual cloud properties (Feingold et al., 2021). Here we address this challenge by adapting techniques from the cloud-feedback literature. We develop a cloud radiative kernel that separates the radiative anomalies caused by changes in r_e, LWP, and liquid-cloud amount, and we relate each of these radiative anomalies to local aerosol concentrations and N_d. This facilitates an assessment of the Twomey effect and liquid-cloud adjustments over the global ocean.

2 Data and Methods

2.1 Satellite Data, Reanalysis, and Climate Model Output

We analyze monthly gridded satellite observations from 2003 through 2020 obtained from the Moderate Imaging Spectroradiometer (MODIS) MCD06COSP dataset version 6.2.0 (Pincus et al., 2023). This dataset combines observations from MODIS instruments onboard the Aqua and Terra satellites. Our primary unit of analysis is a joint histogram of liquid-topped cloud fraction partitioned by r_e and LWP (Fig. 1a). These histograms represent the fractional occurrence of liquid-topped clouds that are exposed to space, hence they do not include cases where liquid cloud is obscured by overlying ice. LWP is defined by the vertical integral of cloud liquid water mass per unit area, and r_e is defined by the ratio of the third and second moments of the cloud-droplet radius distribution. These two variables are estimated with the MODIS 3.7 μm retrieval algorithm (Platnick et al., 2017).

We also use daily gridded N_d estimates from MODIS (Gryspeerdt et al., 2022) and monthly gridded radiative flux retrievals from the Cloud and the Earth's Radiant Energy System (CERES) Energy Balanced and Filled ed. 4.1 and FluxByCldTyp ed. 4.1 datasets (Loeb et al., 2018; Sun et al., 2022). The MODIS N_d estimates can be biased when r_e is

sufficiently small, when the cloud visible optical thickness is sufficiently small, or when three-dimensional radiative transfer effects contribute to the measured radiances (Grosvenor et al., 2018). To avoid these problematic cases, N_d is estimated for liquid clouds that satisfy several conditions: (i) a single cloud layer is present, (ii) $r_e > 4\ \mu m$, (iii) cloud optical thickness is

65 larger than four, (iv) cloud fraction at 5 km resolution is larger than 0.9, (v) the solar zenith angle is less than 65°, (vi) the satellite viewing zenith angle is less than 55°, (vii) the sub-pixel heterogeneity index defined by Zhang and Platnick (2011) is less than 0.3, and (viii) cloud optical thickness is in the top 10% of values in 100 km × 100 km regions. The final condition preferentially selects the convective cores in cloudy scenes (Zhu et al., 2018). Most cloud droplets in shallow convective clouds form near the cloud base, so N_d in convective cores is an indicator of the CCN concentration in air that enters the

70 cloud from below (Rosenfeld et al., 2019). For consistency with the MODIS cloud histograms, we use N_d estimates from the MODIS 3.7 μm retrieval algorithm, and we combine data from the Terra and Aqua satellites. Daily values of $\ln N_d$ are averaged across the satellite platforms and over one-month intervals, weighted by the number of pixels with a valid N_d retrieval.

Monthly meteorological fields and the dry mass concentration of sulfate aerosol at 910 hPa, s, are obtained from

75 MERRA-2 reanalysis (Gelaro et al., 2017; Randles et al., 2017). We consider sulfate aerosol because it dominates the anthropogenic influence on CCN (Charlson et al., 1992; Stevens, 2015), and we select data from 910 hPa rather than the surface because the 910 hPa level is a better indicator of aerosol concentration near cloud base (Painemal et al., 2017). The sulfate data are determined from bias-corrected observations of total aerosol optical depth from cloud-free pixels and simulations from a global model that treats the sources, sinks, and chemistry of sulfate and its precursor gases. The data

80 assimilation accounts for aerosol swelling in humid environments and filters out pixels near clouds that are affected by retrieval bias (Randles et al., 2017). The main limitation of the sulfate data is that the total aerosol optical depth is constrained by observations, but aerosol species distributions and vertical profiles are not. These data provide an additional indicator of cloud-base CCN concentration that is independent of the MODIS estimates of N_d.

Finally, we use output from historical simulations of 20 global climate models (GCMs) from the Coupled Model

85 Intercomparison Project Phase 6 (CMIP6). The simulations are run from 1850 through 2014 with realistic emissions of greenhouse gases, aerosols, and aerosol precursor gases. Sulfate mass concentration from the model output is converted to pressure coordinates and linearly interpolated to 910 hPa. The models are listed in Supplementary Table 1.

2.2 Quantifying Aerosol Indirect Effects

We first relate variability of aerosols to the radiative effects of liquid clouds – relationships we call "aerosol indirect

90 effects." Our analysis begins with the MODIS joint histograms of liquid-cloud fraction, C, partitioned by r_e and LWP (Fig. 1a). Shortwave (SW) radiative flux anomalies induced by liquid clouds, R', are estimated according to

$$R' = \sum_{r=1}^{6} \sum_{l=1}^{7} C'_{rl} \frac{\partial R}{\partial C_{rl}},$$

3

where r and l represent the r_e and LWP dimensions of the histogram and primes denote monthly anomalies relative to the climatological seasonal cycle. The cloud radiative kernel, $\partial R/\partial C_{rl}$, represents that change in top-of-atmosphere SW flux that would occur if the cloud fraction C_{rl} were to increase by 1% with all non-cloud factors fixed (Fig. 1b). The kernel is computed with the Rapid and Accurate Radiative Transfer Model for Global Climate Models (Clough et al., 2005) following a method similar to that of Zelinka et al. (2012). We then adapt a method of cloud-feedback analysis developed by Zelinka et al. (2013) to decompose R' into contributions from different cloud properties:

$$R' = R'_{r_e} + R'_{\mathrm{LWP}} + R'_{\mathrm{CF}} + R'_{\mathrm{res}}.$$

R'_{r_e}, R'_{LWP}, and R'_{CF} are the SW flux anomalies caused by r_e, LWP, and cloud-amount anomalies, respectively – each computed with the other properties held fixed. R'_{res} is the residual of the decomposition. The methods for computing the kernel and decomposing R' are described in Appendix A and B.

To test robustness of the results, we make one set of R' estimates in which only fully cloudy pixels are included in the histograms and a second set of estimates in which fully and partly cloudy pixels are both included. We refer to these cases as MODIS_CLD and MODIS_CLD+PCL, respectively. The filter of the MODIS_CLD case avoids retrieval biases that affect partly cloudy pixels, but it may introduce a sampling bias by excluding some cloud elements. The opposite is true for MODIS_CLD+PCL. Both cases are presented to explore tradeoffs between the accuracy and completeness of the satellite cloud data.

We relate R' to sulfate and cloud-droplet concentrations using cloud-controlling factor analysis (Scott et al., 2020; Myers et al., 2021). Our analysis closely follows the method of Wall et al. (2022), except that we generalize their results by applying cloud-controlling factor analysis to R' and each of its components. The cloud-controlling factor method approximates R' as a linear combination of seven local cloud-controlling factors x_i:

$$R' \approx \sum_{i=1}^{7} \frac{\partial R}{\partial x_i} x_i'.$$

The first six x_i terms include sea surface temperature, estimated inversion strength at the top of the planetary boundary layer (Wood and Bretherton, 2006), low-level advection across a surface-temperature gradient, surface wind speed, relative humidity at 700 hPa, and vertical wind at 700 hPa. Collectively these terms represent all of the main large-scale meteorological controls on liquid clouds in the marine boundary layer that have been proposed in the literature (Scott et al., 2020). The final x_i term can be either $\ln s$ or $\ln N_d$. All meteorological terms and $\ln s$ are calculated with MERRA-2 data and linearly interpolated to the native $1° \times 1°$ grid of MODIS. We then select ocean-covered grid boxes, remove the climatological seasonal cycle and linear trend from all variables, and average the anomalies over a $5° \times 5°$ grid that spans 55°S to 55°N. For each ocean grid box, R' is regressed against anomalies of the seven cloud-controlling factors using ordinary least-squares multilinear regression. Separate regressions are performed with $\ln s$ and $\ln N_d$ as the final predictor. Thus, the regression coefficients $\partial R/\partial \ln s$ and $\partial R/\partial \ln N_d$ represent the relationship between R' and local anomalies of $\ln s$ or $\ln N_d$ with all meteorological predictors held constant. On average, the regression method explains 46% of the variance of

125 R' when $\ln s$ is the final predictor and 49% of the variance when $\ln N_d$ is the final predictor. We also apply the method to R'_{r_e}, R'_{LWP}, and R'_{CF} to estimate the Twomey effect, LWP adjustment, and cloud-fraction adjustment. Finally, we note that our method is slightly different than that of Wall et al. (2022) because we consider all liquid-topped clouds, while they consider clouds that have tops between the surface and 680 hPa.

Our analysis differs from existing global estimates of aerosol indirect effects in several ways. First, estimates that

130 control for fewer meteorological factors are susceptible to bias from correlations between meteorology and aerosols (Mauger and Norris, 2007; Gryspeerdt et al., 2016; Andersen et al., 2017). Our method minimizes this bias by controlling for all of the main large-scale meteorological drivers of liquid boundary-layer clouds that have been proposed in the literature. Second, estimates derived from daily or monthly grid-box averages of r_e and LWP suffer from aggregation bias because these properties are nonlinearly related to cloud albedo (Feingold et al., 2021; Gryspeerdt et al., 2019). Our method avoids

135 this bias by inferring cloud radiative effects from joint histograms of r_e and LWP rather than grid-box averages. Third, studies of ship tracks, industrial plumes, or volcanic eruptions offer some of the most captivating evidence of aerosol indirect effects, but the estimates they provide may not be representative of the global scale (Possner et al., 2018; Toll et al., 2019; Glassmeier et al., 2021). Our method avoids this potential sampling bias by estimating aerosol indirect effects across the global ocean. Fourth, no global observational study has simultaneously estimated the Twomey effect, LWP adjustment, and

140 cloud-fraction adjustment, so comparisons of these components have been complicated by the fact that each one is estimated using different data, methods, assumptions, and uncertainty quantification (Forster et al., 2021). Our method avoids this complication by estimating all components with a single, self-consistent framework. Our estimates of aerosol indirect effects could still be affected by satellite retrieval biases, but they improve upon existing estimates in these four ways (Painemal and Zuidema, 2011; Ma et al., 2018).

145 **3 Global Analysis of Aerosol Indirect Effects**

We next present estimates of the Twomey effect and cloud adjustments across the global ocean. The Twomey effect can occur whenever the CCN concentration is small enough that it limits the number of droplets that form in cloud updrafts. This condition is usually satisfied over ocean, so the Twomey effect is expected to be ubiquitous in oceanic clouds (Rosenfeld et al., 2014). Indeed, we find that increasing sulfate concentration is associated with significant cloud brightening

150 from R_{r_e} changes across most of the global ocean (Fig. 2a). Cloud brightening is also observed in response to increasing N_d (Fig. 2b), but we caution against overinterpreting statistical significance of this relationship because R_{r_e} and N_d are both inferred from the MODIS r_e retrievals (N_d is inferred using 10% of the data). Nevertheless, these results show that most marine liquid clouds exhibit the Twomey effect.

In contrast, previous work has shown that cloud adjustments can differ from one cloud regime to another. As cloud

155 droplets become smaller, they sediment more slowly out of the cloud-top entrainment zone, and they evaporate more quickly when exposed to entrained air. This enhances evaporation and reduces LWP in non-precipitating clouds (Bretherton et al.,

2007; Small et al., 2009). Clouds with smaller droplets also form precipitation more slowly through collision and coalescence. This may cause other changes in cloud properties, including deeper cumulus clouds, longer cloud lifetimes, larger stratiform areas detrained from precipitating cloud elements, or changes in mesoscale cellular structure (Albrecht,

160   1989; Pincus and Baker, 1994; Rosenfeld et al., 2006; Seifert et al., 2015; Possner et al., 2018; Dagan et al., 2017; Goren et al., 2022). The cloud adjustments can, in turn, affect CCN concentration by changing precipitation scavenging or sulfate formation in cloud droplets (Wood et al., 2012; Kang et al., 2022; Andreae and Rosenfeld, 2008). Some of these mechanisms depend on the meteorological conditions, so they may vary regionally (Chen et al., 2014).

The estimated cloud adjustments exhibit regional variations that are consistent with some of these proposed

165   mechanisms. The radiative adjustment from LWP changes is positive in much of the subtropics, and it maximizes in areas of semi-permanent stratocumulus clouds and directly downwind (Fig. 2c-d). This spatial pattern suggests that enhanced evaporation in non-precipitating stratocumulus may contribute to the LWP adjustment. The radiative adjustment from cloud-fraction changes is negative in most of the subtropics and midlatitudes, so the adjustment may involve changes in cloud lifetime, size, or morphology as well (Fig. 2e-f). Subtropical stratocumulus regions exhibit both of these adjustments

170   simultaneously. In these cases, as CCN become more abundant, the overall liquid-cloud fraction increases, but the increase is disproportionately large in cloud elements with below-average LWP. This combination is consistent with larger stratiform areas detrained from precipitating clouds or a shift from open to closed mesoscale cellular convection (Possner et al., 2018; Rosenfeld et al., 2006). Thus, aerosol-driven changes in evaporation and precipitation may both contribute to cloud adjustments. The spatial patterns of the adjustments predicted with $\ln s$ resemble those predicted with $\ln N_d$, suggesting that

175   the estimated adjustments are robust.

We determine the relative importance of the Twomey effect and cloud adjustments at the global scale by averaging the regression coefficients over ocean. These averages can be interpreted as the cloud radiative anomalies that would occur if sulfate concentration and N_d were increased by a factor of 2.7 at every location. Uncertainty quantification for these estimates is described in Appendix C. For the regressions against $\ln s$ and $\ln N_d$, we find that the Twomey effect and cloud-

180   fraction adjustment both significantly increase SW reflection to space (Fig. 3). The cloud-fraction adjustment enhances SW reflection by between 43% and 250% compared to the Twomey effect alone (95% CI), so it makes a substantial contribution to the overall aerosol indirect effect. The large relative magnitude of the cloud-fraction adjustment is consistent with the observed cloud response during a volcanic eruption in Holuhraun, Iceland, and the uncertainty range for this adjustment overlaps with other observational estimates (Chen et al., 2022; Gryspeerdt et al., 2020). The LWP adjustment offsets

185   between 6% and 87% of the Twomey effect, but the total cloud adjustment is still comparable to the Twomey-effect component. Furthermore, the estimated Twomey effect and total cloud adjustment are similar for the MODIS$_{CLD}$ and MODIS$_{CLD+PCL}$ cases, indicating that they do not change substantially when partly cloudy pixels are filtered in different ways. The Twomey effect and total cloud adjustment are also qualitatively consistent when different N_d datasets are used, and they are an order of magnitude larger than $\partial R_{res}/\partial \ln s$ and $\partial R_{res}/\partial \ln N_d$ (Supplementary Fig. 1 and 2). These results

190   robustly show that the Twomey effect and total cloud adjustment cause comparable changes in top-of-atmosphere SW flux.

A limitation of these results is that the MODIS$_\text{CLD}$ and MODIS$_\text{CLD+PCL}$ cases have offsetting differences in the estimated LWP and cloud-fraction adjustments (Fig. 3). This means that estimates of the individual LWP and cloud-fraction adjustments depend on filtering of partly cloudy pixels, but the estimate of the total cloud adjustment does not. One implication is that aerosol variations must be associated with changes in the relative amounts of partly and fully cloud-

195 covered pixels. These pixels reside on cloud edges and interiors, respectively, so a change in the relative amounts of the pixel categories implies a change in the cloud perimeter-to-area ratio (Wall et al., 2022). This suggests that the global cloud adjustment may involve changes in cloud size or morphology. A case study demonstrating this concept is presented in Appendix D. A second implication is that the conventional practice of estimating the individual LWP and cloud-fraction adjustments at the global scale will inevitably lead to results that depend on the classification and filtering of partly cloudy

200 pixels. Thus, instrument sensitivity, horizontal resolution, and subjective pixel-classification thresholds can all affect the results. In contrast, we find that more robust results can be obtained by estimating the total cloud adjustment. Our analysis provides the first direct assessment of this quantity from observations and reanalysis.

4 Implications for Historical Aerosol Forcing

We next combine estimates of aerosol indirect effects and historical sulfate changes to infer ERF$_\text{aci}$. The forcing
205 estimates use sulfate rather than N_d because sulfate concentration is a widely available output variable from GCMs, but N_d filtered by cloud optical thickness is not. Assuming that sulfate dominates the anthropogenic influence on CCN (Charlson et al., 1992; Stevens 2015), the SW ERF$_\text{aci}$ from liquid-topped clouds can be estimated by

$$\text{ERF}_\text{aci} \approx \frac{\partial R}{\partial \ln s} \Delta \ln s$$

where $\Delta \ln s$ is the sulfate change between preindustrial (1850-1859) and present-day (2005-2014) conditions. Estimates of
210 $\Delta \ln s$ are obtained from GCMs that participated in CMIP6. This method of estimating ERF$_\text{aci}$ has been validated with volcanic eruptions and other known variations of regional sulfur-dioxide emissions (Wall et al., 2022).

The method can be applied to each component of the aerosol indirect effect to estimate the associated historical effective radiative forcing. The Twomey effect contributes a negative instantaneous radiative forcing (IRF$_\text{aci}$) that peaks in subtropical stratocumulus regions and the midlatitude oceans of the Northern Hemisphere (Fig. 4a). Forcing is relatively
215 large in stratocumulus regions because these clouds exhibit a strong radiative response to CCN perturbations (Fig. 2), and forcing is relatively large in the Northern Hemisphere midlatitudes because these regions are close to anthropogenic aerosol sources. The geographic pattern and magnitude of the IRF$_\text{aci}$ generally agree with the estimates of McCoy et al. (2017), Kinne (2019), and Jia et al. (2021). Furthermore, the IRF$_\text{aci}$ is comparable to the effective radiative forcing from the combined effect of LWP adjustments (A$_\text{LWP}$) and cloud-fraction adjustments (A$_\text{CF}$) (Fig. 4b). Thus, the magnitude of the
220 overall ERF$_\text{aci}$ also peaks in the subtropical stratocumulus regions and the Northern Hemisphere midlatitudes (Fig. 4c).

7

We average the forcing components over ocean between 55°S and 55°N to quantify their large-scale climate impacts. Confidence intervals are computed accounting for regression-slope uncertainty and inter-model spread in the estimates of $\Delta \ln s$ (Appendix C). To frame our results in the context of the existing literature, we compare our estimates with forcing calculations from an assessment of the World Climate Research Programme (WCRP) (Bellouin et al., 2020) and

225   forcing estimates from 14 GCMs that participated in the Coupled Model Intercomparison Project Phase 5 (CMIP5) and AeroCom Indirect Effect experiments computed by Gryspeerdt et al. (2020) (Supplementary Table 1). We repeat the original WCRP analysis, except that we restrict the calculation to SW forcing over ocean between 55°S and 55°N, as described in the Supplementary Information. The GCM forcing estimates are averaged over ocean between 55°S and 55°N as well. Although all forcing estimates are computed over the same spatial domain, their time periods differ slightly from one another: The

230   present-day reference years are 2005-2014 for our estimates, 2005-2015 for the WCRP estimates, and 2000 for the CMIP5 and AeroCom estimates, and the preindustrial reference years are 1850-1859 for our estimates, 1850 for the WCRP and CMIP5 estimates, and 1860 for the AeroCom estimates (Bellouin et al., 2020; Zelinka et al., 2014; Ghan et al., 2016). These differences in the reference periods could cause differences in ERF$_{aci}$ of 0.1 W m^{-2} or less (IPCC, 2021).

Averages of IRF$_{aci}$, cloud adjustments, and the overall ERF$_{aci}$ are compared in Fig. 5. We find that A$_{CF}$ is

235   significantly negative, and A$_{LWP}$ is more likely than not to be positive, but the magnitudes of these estimates depend on filtering choices for partly cloudy pixels. The three remaining components are insensitive to partly-cloudy-pixel filtering: the IRF$_{aci}$ is -0.77 ± 0.25 W m^{-2}, the total cloud adjustment is -1.02 ± 0.43 W m^{-2}, and the overall ERF$_{aci}$ is -1.86 ± 0.62 W m^{-2} (95% CIs from MODIS$_{CLD}$). These results lie inside the ranges of the corresponding WCRP and GCM estimates, and the median IRF$_{aci}$ agrees very well with the WCRP and GCM values. However, our results reduce uncertainty of each

240   component by at least 62% relative to the confidence intervals of the WCRP and at least 23% relative to the range of GCMs. Furthermore, the WCRP and GCM estimates do not rule out the possibility that the total cloud adjustment is positive or an order of magnitude smaller than the IRF$_{aci}$. According to our analysis, however, such a small or positive adjustment is implausible. Thus, our findings reduce uncertainty in the historical IRF$_{aci}$ and total cloud adjustment, and they clarify the relative importance of these components.

245   The ocean-average SW ERF$_{aci}$ can be scaled to establish an upper bound for the global-average net ERF$_{aci}$. Let ERF$_{aci,net,g}$ be the global-average net ERF$_{aci}$, and let ERF$_{aci,net,d}$ be the domain-average net ERF$_{aci}$, where the domain includes ocean areas between 55°S and 55°N. Assuming that the average net ERF$_{aci}$ is negative outside the domain (Diamond et al., 2020), it follows that

$$\text{ERF}_{aci,net,g} < f\,\text{ERF}_{aci,net,d} \qquad (1)$$

where $f = 0.56$ is the fraction of global surface area covered by the domain. ERF$_{aci,net,d}$ can be expressed as

$$\text{ERF}_{aci,net,d} = \text{ERF}_{aci,sw,d}(1 - \beta) \qquad (2)$$

250   where ERF$_{aci,sw,d}$ is the domain-average SW ERF$_{aci}$ and β is the fraction of SW ERF$_{aci}$ that is offset by longwave ERF$_{aci}$. Our radiative kernel cannot accurately assess longwave cloud radiative effects, so β is estimated by applying cloud-controlling

factor analysis to CERES satellite data instead (Appendix B). The resulting uncertainty range is $\beta = 0.14 \pm 0.06$ (90% CI). We evaluate equation (2) with the bounds of the 90% CIs of β and $\text{ERF}_{\text{aci,sw,d}}$ from the MODIS$_{\text{CLD}}$ and MODIS$_{\text{CLD+PCL}}$ cases, then select the least-negative value of $\text{ERF}_{\text{aci,net,d}}$ to evaluate inequality (1). The result constitutes an upper bound for

255　　$\text{ERF}_{\text{aci,net,g}}$.

　　　　The above reasoning implies a 95% probability that the global net ERF_{aci} from liquid clouds is more negative than -0.56 W m^{-2} (relative to 1850-1859). Equivalent upper bounds from the published literature include -0.07 W m^{-2} from the WCRP assessment and -0.3 W m^{-2} from the observation-based estimate of the IPCC Sixth Assessment Report (relative to 1850 and 1750, respectively) (Bellouin et al., 2020; Forster et al., 2021). Our analysis thus supports a more stringent upper

260　　bound on global ERF_{aci}. This constraint is similar to another estimate from cloud-controlling factor analysis presented by Wall et al. (2022), but our estimate invokes weaker assumptions because it does not extrapolate forcing to areas outside the domain. Our upper-bound estimate also complements evidence from global energy-balance arguments, which constrains the lower bound of ERF_{aci} (Stevens et al., 2015; Smith et al., 2021).

5 Conclusion

265　　　　We analyze MODIS satellite data and adapt cloud radiative kernels and cloud-controlling factor analysis from the cloud-feedback literature to quantify aerosol indirect effects from liquid-topped clouds (Zelinka et al., 2012; Zelinka et al., 2013; Scott et at., 2020; Myers et al., 2021). Our method avoids aggregation and sampling biases that may affect some previous studies, and it controls for all of the main large-scale meteorological drivers of liquid boundary-layer clouds that have been proposed in the literature, thereby minimizing biases in estimated aerosol-cloud relationships that arise from

270　　confounding meteorological factors (Possner et al., 2018; Glassmeier et al., 2021; Feingold et al., 2021). Importantly, the Twomey effect, LWP adjustment, and cloud-fraction adjustment are simultaneously quantified with a single, self-consistent framework. This guarantees that all of the components, and their uncertainties, are quantified in a consistent way. Although it will be important to continue characterizing satellite retrieval biases, to include new meteorological cloud-controlling factors as they are discovered, and to quantify additional ERF_{aci} components from ice-containing clouds, our method clarifies

275　　the relative importance of the Twomey effect and liquid-cloud adjustments across the global ocean.

　　　　We find that increasing CCN concentration is associated with widespread cloud brightening from the Twomey effect, a positive radiative adjustment from decreasing LWP in subtropical stratocumulus regions, and a negative radiative adjustment from increasing cloud fraction in the subtropics and midlatitudes. The estimated aerosol indirect effects are combined with historical sulfate changes from CMIP6 models to quantify the associated SW ERF_{aci}. The Twomey effect and

280　　total cloud adjustment contribute -0.77 ± 0.25 W m^{-2} and -1.02 ± 0.43 W m^{-2}, respectively, to the mean ERF_{aci} over ocean between 55°S and 55°N (95% CIs). Our findings reduce uncertainty in these forcing components and suggest that liquid-cloud adjustments make a larger contribution to historical aerosol forcing than is commonly believed.

Appendix A: Cloud Radiative Kernel

We compute a SW cloud radiative kernel for the MODIS r_e-LWP joint histogram to quantify the effect of liquid-cloud anomalies on the top-of-atmosphere SW flux. The radiative kernel is similar to that of Zelinka et al. (2012) with two exceptions. First, our kernel represents liquid-topped clouds, while their kernel represents clouds of all phases. Second, our kernel is partitioned by r_e and LWP, while their kernel is partitioned by cloud-top pressure and cloud optical thickness. Besides these exceptions, we calculate the kernel by closely following the method of Zelinka et al. (2012).

The first step of the kernel calculation is to quantify the clear-sky upward SW flux at the top of the atmosphere for various combinations of surface albedo, latitude, and calendar month. Calculations are performed with the Rapid and Accurate Radiative Transfer Model for Global Climate Models (Clough et al., 2005) using inputs that include the climatological seasonal cycle of humidity from MERRA-2, a standard ozone profile, and a solar constant of 1361 W m^{-2}. For a given latitude and month, we chose a day in the middle of the month and calculate the average of the cosine of the solar zenith angle μ_i for each one-hour interval throughout the day. We then scale μ_i by $SW_{\downarrow,\text{CERES}}/SW_{\downarrow,\text{day}}$, where $SW_{\downarrow,\text{day}}$ is the daily-mean insolation for the day in the middle of the month and $SW_{\downarrow,\text{CERES}}$ is the monthly-mean insolation from CERES satellite data (Loeb et al. 2018). This step ensures that the monthly-mean insolation for the radiative kernel is equal to that of CERES. We compute the clear-sky SW flux for each of the 24 μ_i terms, then average the results. The calculations are performed using surface albedo of 0, 0.5, and 1. The final result is a matrix of clear-sky upward SW flux at the top of the atmosphere as a function of surface albedo, latitude, and calendar month.

The next step is similar to the clear-sky calculations except that an overcast and horizontally uniform liquid cloud is introduced in the radiation code. The r_e and LWP of the cloud are varied, and cloud-top pressure is prescribed to 850 hPa to match the modal value retrieved by MODIS. For r_e, we use the standard MODIS retrieval algorithm, $r_{e,\text{std}}$, and the 3.7 μm retrieval algorithm, $r_{e,3.7}$. Monthly gridded values of $r_{e,\text{std}}$ and $r_{e,3.7}$ have a correlation coefficient of 0.92 over ocean, but they are generally different because $r_{e,3.7}$ represents conditions closer to the cloud top (Platnick, 2000). We therefore prescribe r_e inside the cloud as

$$r_e = \begin{cases} r_{e,3.7}, & \tau_c < 3 \\ \tilde{r}_{e,\text{std}}, & \tau_c \geq 3 \end{cases}$$

where τ_c is the visible optical depth below cloud top and $\tilde{r}_{e,\text{std}} \equiv mr_{e,3.7} + b$, where $m = 1.14$ and $b = -0.35$ μm. The coefficients m and b are determined by regressing $r_{e,\text{std}}$ against $r_{e,3.7}$ using all monthly $1° \times 1°$ ocean grid boxes, and the $\tau_c = 3$ threshold is chosen from weighting functions estimated by Platnick (2000). Using these relationships, we calculate the top-of-atmosphere SW flux with different combinations of $r_{e,3.7}$ and LWP that correspond to the bins of the MODIS r_e-LWP joint histogram. Separate calculations are performed for synthetic clouds at the four edges of each bin, and the results are averaged to get one value of upward SW flux at the top of the atmosphere for each bin. We then subtract the resulting value from the clear-sky upward SW flux to determine the SW cloud radiative effect (CRE). These calculations produce a matrix of SW CRE above an overcast liquid cloud as a function of latitude, surface albedo, calendar month, r_e, and LWP.

The final step of the calculation is to convert the overcast-sky SW CRE to a cloud radiative kernel, K. Let C_{rl} be the liquid-cloud fraction in effective radius bin r and LWP bin l. The K matrix represents how anomalies of C_{rl} affect R with all non-cloud factors fixed:

$$K_{rl} \equiv \frac{\partial R}{\partial C_{rl}}.$$

K_{rl} is computed by dividing the overcast-sky SW CRE by 100%. We apply linear interpolation to transform K_{rl} from latitude-surface-albedo space to latitude-longitude space using the climatological seasonal cycle of surface albedo from CERES. The final radiative kernel has units of W m^{-2} %$^{-1}$ and is a function of latitude, longitude, calendar month, r_e, and LWP (Fig. 1b).

We validate the radiative kernel by comparing R' observations from the CERES FluxByCldTyp dataset (Sun et al., 2022) with R' estimates derived from the kernel and MODIS r_e-LWP joint histograms. The kernel estimates are regressed against the CERES observations using data from all monthly $1° \times 1°$ ocean gridboxes between 55°S and 55°N from 2003 through 2020. The regression slope is 1.046 ± 0.005 (95% CI) (Figure A1). This means that biases of our radiative kernel and differences between the MODIS and CERES cloud retrieval algorithms cause the kernel-based estimate of R' to overestimate its CERES counterpart by $+4.6 \pm 0.5\%$.

Appendix B: Decomposing Cloud Radiative Effects

For a given latitude, longitude, and month, the total liquid-cloud-induced SW flux anomaly at the top of the atmosphere, R', is

$$R' = \sum_{r=1}^{6} \sum_{l=1}^{7} K_{rl} C_{rl}' \tag{B1}$$

We decompose the term on the right side of equation B1 to estimate how much cloud-amount anomalies, r_e anomalies, and LWP anomalies contribute to R'. The decomposition closely follows the method described in Appendix B of Zelinka et al., (2013), except that our radiative kernel and histogram have different dimensions.

First, let C_{tot} be the total liquid-cloud fraction summed over all r_e-LWP bins. We express C_{rl}' as

$$C_{rl}' = \frac{\bar{C}_{rl}}{\bar{C}_{\text{tot}}} C_{\text{tot}}' + C_{rl}^* \tag{B2}$$

where overbars denote values from the climatological seasonal cycle. The first term on the right side of equation B2 represents the anomalies of C_{rl} that would occur if C_{tot}' were distributed among the r_e-LWP bins such that the normalized distribution in the histogram remains the same as the climatology. In other words, this term accounts for a change in total liquid-cloud fraction, holding fixed the proportion of clouds in each histogram bin. The second term on the right side of equation B2 accounts for anomalies of C_{rl} that remain after removing $(\bar{C}_{rl}/\bar{C}_{\text{tot}})C_{\text{tot}}'$. This term represents shifts in the

distribution of r_e and LWP with the total liquid-cloud fraction fixed. By construction, C_{rl}^* vanishes when it is summed over all histogram bins.

Next, we decompose the radiative kernel into two terms:

$$K_{rl} = K_0 + \widehat{K}_{rl}. \tag{B3}$$

Here, K_0 is the average of K_{rl} weighted by cloud fraction,

$$K_0 \equiv \sum_{r=1}^{6} \sum_{l=1}^{7} \frac{\bar{C}_{rl}}{\bar{C}_{\text{tot}}} K_{rl}, \tag{B4}$$

345 and $\widehat{K}_{rl} \equiv K_{rl} - K_0$. With the relationships defined in equations B1-B4, R' can be expressed as

$$R' = K_0 C_{\text{tot}}' + \sum_{r=1}^{6} \sum_{l=1}^{7} \widehat{K}_{rl} C_{rl}^*.$$

We next decompose $\widehat{K}_{rl}$ into three components:

$$\widehat{K}_{rl} = \widehat{K}_r + \widehat{K}_l + \widehat{K}_{\text{res}}$$

where

$$\widehat{K}_r \equiv \sum_{l=1}^{7} \left(\widehat{K}_{rl} \sum_{r=1}^{6} \frac{\bar{C}_{rl}}{\bar{C}_{\text{tot}}} \right),$$

$$\widehat{K}_l \equiv \sum_{r=1}^{6} \left(\widehat{K}_{rl} \sum_{l=1}^{7} \frac{\bar{C}_{rl}}{\bar{C}_{\text{tot}}} \right),$$

and

$$\widehat{K}_{\text{res}} \equiv \widehat{K}_{rl} - \widehat{K}_r - \widehat{K}_l.$$

350 R' can then be expressed as

$$R' = K_0 C_{\text{tot}}' + \sum_{r=1}^{6} \left(\widehat{K}_r \sum_{l=1}^{7} C_{rl}^* \right) + \sum_{l=1}^{7} \left(\widehat{K}_l \sum_{r=1}^{6} C_{rl}^* \right) + \sum_{r=1}^{6} \sum_{l=1}^{7} \widehat{K}_{\text{res}} C_{rl}^*. \tag{B5}$$

The first term on the right side of equation B5 is the SW flux anomaly that would occur if the anomaly of total liquid-cloud fraction were distributed among the r_e-LWP bins such that the proportion of cloud fraction in each bin is the same as the climatology. This term represents the contribution of cloud-amount anomalies to R'. The second term on the right side results from multiplying an effective kernel that accounts for systematic variations in r_e by the change in cloud fraction at each r_e

355 bin. This term represents the contribution of r_e anomalies to R' with LWP and total liquid-cloud fraction held fixed. The third term on the right side is similar to the second term except that it represents the contribution of LWP anomalies to R' with r_e and total liquid-cloud fraction held fixed. The final term on the right is the residual of the decomposition. The cloud-amount, r_e, LWP, and residual components of R' are denoted by R_{CF}', R_{r_e}', R_{LWP}', and R_{res}', respectively. In the Supplementary Information, we validate the R' decomposition using synthetic-data test cases in which R_{r_e}' and R_{LWP}' can be

360   estimated theoretically with the two-stream radiative transfer approximation (Supplementary Fig. 3). We also verify that R'_{r_e}
and R'_{LWP} are similar when different common assumptions are made about cloud vertical structure, including a vertically
uniform cloud model, an adiabatic cloud model, and the two-layer cloud model from the kernel calculation.

         The final step of the decomposition is to adjust R'_{CF} to account for obscuration effects from non-liquid clouds.
Because MODIS is a passive instrument, changes in non-liquid clouds can artificially change the retrieved liquid-cloud
365   fraction if they obscure liquid clouds from the satellite view. We control for these obscuration effects by replacing C'_{tot} in
equation B5 by $[C_{\text{tot}}/(100\% - I_{\text{tot}})]'(100\% - \bar{I}_{\text{tot}})$, where I_{tot} is the retrieved fraction of non-liquid clouds. This change of
variables is adapted from the procedure recommended by Scott et al. (2020).

         We also wish to compare the SW and longwave (LW) components of cloud radiative effects. However, our
radiative kernel assumes a constant cloud-top pressure, so it cannot accurately assess the LW component (Appendix A).
370   Instead, we analyze observations of the SW and LW radiative effects of liquid-topped clouds from the CERES
FluxByCldTyp dataset. We perform cloud-controlling factor analysis with the CERES data to attain estimates of ERF$_{\text{aci}}$ in
addition to those presented in the main paper. The CERES-based estimate of SW ERF$_{\text{aci}}$ averaged over ocean between 55°S
and 55°N is -1.52 ± 0.51 W m^{-2}. The estimated LW ERF$_{\text{aci}}$ over the same domain is $+0.21 \pm 0.13$ W m^{-2} (95% CIs). These
values determine β in the upper-bound estimate of global net ERF$_{\text{aci}}$ (equation 2).

375   **Appendix C: Uncertainty**

         Uncertainty in our ocean-average ERF$_{\text{aci}}$ estimates arises from uncertainty in the regression coefficients
representing $\partial R / \partial \ln s$ and uncertainty in the model estimates of $\Delta \ln s$. We first quantify the component that is attributable
to regression-coefficient uncertainty. For a particular grid box i, let ϵ_i represent the half-width of the 95% confidence
interval of grid-box mean ERF$_{\text{aci}}$. We estimate ϵ_i as

380
$$\epsilon_i = t_i \sigma_i \sqrt{\frac{N_{\text{nom},i}}{N_{\text{eff},i}}} [\Delta \ln s]_i$$

where σ_i is the standard error of the regression coefficient, $N_{\text{nom},i}$ is the nominal number of temporal degrees of freedom,
$N_{\text{eff},i}$ is the effective number of temporal degrees of freedom, square brackets indicate the central estimate of a parameter,
and t_i is the critical value of a Student's t-distribution at the $(1 - \alpha/2)100\%$ significance level using $N_{\text{eff},i} - 8$ degrees of
freedom and $\alpha = 0.05$. The ratio $N_{\text{nom},i}/N_{\text{eff},i}$ is estimated as $(1 + a)/(1 - a)$, where a is the temporal lag-1
385   autocorrelation of R'_i. The ϵ_i terms are then combined to account for spatial averaging over the domain. Uncertainty of the
domain-average forcing, δ_{obs}, is

$$\delta_{\text{obs}} = \frac{\sqrt{\sum_{i=1}^{N^*_{\text{nom}}} w_i^2 \epsilon_i^2}}{\sum_{i=1}^{N^*_{\text{nom}}} w_i} \sqrt{\frac{N^*_{\text{nom}}}{N^*_{\text{eff}}}}$$

where N_{nom}^* is the nominal number of spatial degrees of freedom, N_{eff}^* is the effective number of spatial degrees of freedom, and w_i is the ocean area in grid box i. The ratio $N_{\text{nom}}^*/N_{\text{eff}}^*$ is estimated by applying equation 5 of Bretherton et al. (1999) to the gridded R' data. The resulting value of δ_{obs} represents the half-width of the 95% confidence interval of ERF_{aci} that is attributable to regression-coefficient uncertainty. Confidence intervals for the spatial averages of $\partial R/\partial \ln s$ and $\partial R/\partial \ln N_d$ are calculated similarly.

The second source of uncertainty of ERF_{aci} arises from inter-model spread in the estimates of $\Delta \ln s$. Because we have estimates from 20 climate models, we construct a 95% confidence interval for ERF_{aci} that excludes one model and encompasses the range of the other 19. We first calculate 20 estimates of ERF_{aci} by multiplying $\Delta \ln s$ from each model by $[\partial R/\partial \ln s]$. The half-width of the confidence interval, $\delta_{\ln s}$, is estimated as the minimum of $|c_1 - c_{19}|/2$ and $|c_2 - c_{20}|/2$, where c_1, c_2, c_{19}, and c_{20} are the smallest, second smallest, second largest, and largest values of the 20 ERF_{aci} estimates, respectively. This uncertainty analysis accounts for inter-model differences in aerosol processing, but it does not account for uncertainty in anthropogenic sulfur-dioxide emissions because the climate-model simulations apply the same emission values. However, sulfur-dioxide emissions depend primarily on the sulfur content of fuel rather than the conditions of combustion, so global emission inventories have a relatively small uncertainty of about $\pm 11\%$ (90% CI from Smith et al., 2011). This is expected to cause an equivalent fractional uncertainty in the global burden of anthropogenic sulfate aerosol (Charlson et al., 1992; Stevens, 2015). In contrast, inter-model differences in aerosol processing lead to an uncertainty of $\pm 43\%$ in the anthropogenic change in s over ocean since 1850 (90% CI estimated by computing the interval that includes 18 of the 20 CMIP6 models). Approximating $\delta_{\ln s}$ from inter-model differences is therefore justified. Finally, we note that ERF_{aci} strongly depends on the preindustrial aerosol state, so our estimates are valid as long as the inter-model spread in preindustrial CCN concentration encompasses the true values (Carslaw et al., 2013; Kinne, 2019). The possibility that the CMIP6 models have systematic biases that violate this condition cannot be ruled out at this time.

The estimated δ_{obs} and $\delta_{\ln s}$ represent independent sources of uncertainty, so they are combined in quadrature. The overall 95% confidence interval is given by $\text{ERF}_{\text{aci}} \pm \sqrt{\delta_{\text{obs}}^2 + \delta_{\ln s}^2}$. Confidence intervals for IRF_{aci}, A_{LWP}, A_{CF}, and the total cloud adjustment are calculated similarly.

Appendix D: Filtering of Partly Cloudy Pixels

Different treatments of partly cloudy pixels in the $\text{MODIS}_{\text{CLD}}$ and $\text{MODIS}_{\text{CLD+PCL}}$ cases lead to offsetting differences in the estimated LWP and cloud-fraction adjustments (Fig. 3). One possible explanation for this discrepancy is that CCN anomalies cause changes in the morphology or horizontal size of liquid clouds, thereby changing the relative amounts of partly and fully cloudy pixels (Possner et al., 2018; Rosenfeld et al., 2006). Here we examine a case study to demonstrate this concept.

We analyze instantaneous pixel data from the MODIS MOD06_L2 dataset collection 6.1 (Platnick et al., 2015) obtained during a single overpass of the Terra satellite on September 27, 2019. On this day, Terra measured stratocumulus

420   clouds in the Southeast Pacific Ocean with different forms of mesoscale cellular convection. The clouds in box C in Fig. D1a mostly exhibit closed cells, and the clouds in box O mostly exhibit open cells. We select data from these boxes and bin the liquid-cloud pixels into histograms of cloud fraction partitioned by LWP. Let C_l represent cloud fraction in LWP bin l. In one case, C_l and C_{tot} are computed by counting only the fully cloudy pixels (CLD), and in a second case, C_l and C_{tot} are computed by counting both fully and partly cloudy pixels (CLD+PCL). Box C contains mostly fully cloudy pixels, so the

425   two cases have similar values of C_l and C_{tot} (Fig. D1b). In contrast, box O contains broken clouds that have a smaller horizontal scale, a larger perimeter-to-area ratio, and a larger proportion of partly cloudy pixels. The partly cloudy pixels cover about 13% of the area of box O, and their retrieved LWP is usually smaller than that of the fully cloudy pixels in the box. This causes a difference in C_{tot} and the C_l distribution between the CLD and CLD+PCL cases (Fig. D1c). Filtering of partly cloudy pixels therefore affects the grid-box-level statistics of cloud fraction and LWP in this example.

430   We next examine differences between the cloud-fraction histograms of the two boxes to demonstrate the implications for estimating R'. For the purpose of this demonstration, let the baseline cloud population be defined by the clouds in Box O, and let the cloud-fraction anomalies be defined by the cloud fraction in box C minus the cloud fraction in box O. The baseline and anomalies are indicated by overbars and primes, respectively. C_l' can be decomposed according to

$$C_l' = \frac{\bar{C}_l}{\bar{C}_{\text{tot}}} C_{\text{tot}}' + C_l^*$$

435   where $C_l^* \equiv C_l' - \frac{\bar{C}_l}{\bar{C}_{\text{tot}}} C_{\text{tot}}'$. This decomposition is equivalent to equation B2 except that it is performed on a one-dimensional LWP histogram rather than a two-dimension LWP-r_e joint histogram. The first term on the right side of the equation determines R_{CF}', and the second term determines R_{LWP}'. Compared with the CLD case, the CLD+PCL case has a smaller value of C_{tot}' (Fig. D1d), which reduces the magnitude of R_{CF}'. Furthermore, because the partly cloudy pixels in box O occupy the smallest LWP bins, including these pixels in the cloud histogram causes a less extreme shift in the C_l' distribution

440   towards small LWP values. This reduces the magnitude of R_{LWP}' in the CLD+PCL case relative to that of the CLD case. Thus, including partly cloudy pixels in the cloud histograms leads to offsetting changes in R_{CF}' and R_{LWP}' that reduce the magnitude of both terms. Our estimates of global cloud adjustments depend on filtering of partly cloudy pixels in a similar way, suggesting that the adjustments may involve changes in cloud size or morphology as well.

Code Availability

445   Matlab code used to analyze data can be obtained by contacting the corresponding author. The Rapid and Accurate Radiative Transfer Model for GCMs is publicly available at http://rtweb.aer.com/rrtm_frame.html.

Data Availability

All satellite data, reanalysis, and GCM output used in this study are publicly available. MODIS cloud histograms are available at https://ladsweb.modaps.eosdis.nasa.gov/archive/allData/62/, MODIS N_d data are available at
450 https://catalogue.ceda.ac.uk/uuid/864a46cc65054008857ee5bb772a2a2b, CERES data are available at https://ceres.larc.nasa.gov/data/, MERRA-2 data are available at https://disc.gsfc.nasa.gov/, and CMIP6 output is available at https://esgf-node.llnl.gov/projects/cmip6/.

Author Contribution

CJW designed research, performed research, analyzed data, and wrote the original paper draft. TS and AP contributed ideas
455 that shaped the study. All authors helped revise the original paper draft.

Competing Interests

The authors declare that they have no conflict of interest.

Acknowledgements

References

Albrecht, B. A.: Aerosols, cloud microphysics, and fractional cloudiness. *Science*, *245*(4923), 1227–1230. https://doi.org/10.1126/science.245.4923.1227, 1989.
465 Andersen, H., et al.: Understanding the drivers of marine liquid-water cloud occurrence and properties with global observations using neural networks. *Atmos. Chem. Phys.*, *17*(15), 9535–9546. https://doi.org/10.5194/acp-17-9535-2017: 2017.
Andreae, M. O., and Rosenfeld, D.: Aerosol-Cloud-Precipitation Interactions Part 1: The Nature and Sources of Cloud-Active Aerosols. *Earth-Sci. Rev.*, *89*(1–2), 13–41. https://doi.org/10.1016/j.earscirev.2008.03.001, 2008.
470 Bellouin, N., et al.: Bounding Global Aerosol Radiative Forcing of Climate Change. *Rev. Geophys.*, 1–45. https://doi.org/10.1029/2019rg000660, 2020.

16

Bretherton, C. S., Blossey, P. N., and Uchida, J.: Cloud Droplet Sedimentation, Entrainment Efficiency, and Subtropical Stratocumulus Albedo. *Geophys. Res. Lett.*, *34*(3), 1–5. https://doi.org/10.1029/2006GL027648, 2007.

Bretherton, C. S., et al.: Effective Number of Degrees of Freedom of a Spatial Field. *J. Clim.*, *12*(1969), 1990–2009. https://doi.org/Doi10.1175/1520-0442(1999)012<1990:Tenosd>2.0.Co;2, 1999.

Carslaw, K. S., et al.: Large contribution of natural aerosols to uncertainty in indirect forcing. *Nature*, *503*(7474), 67–71. https://doi.org/10.1038/nature12674, 2013.

Charlson, R. J., et al.: Climate Forcing by Anthropogenic Aerosols. *Science*, *255*(5043), 423–430. https://doi.org/10.1126/science.255.5043.423, 1992.

Chen, Y. C., et al.: Satellite-Based Estimate of Global Aerosol-Cloud Radiative Forcing by Marine Warm Clouds. *Nat. Geosci.*, *7*(9), 643–646. https://doi.org/10.1038/ngeo2214, 2014.

Chen, Y., et al.: Machine Learning Reveals Climate Forcing from Aerosols is Dominated by Increased Cloud Cover. *Nat. Geosci.*, *15*(8), 609–614. https://doi.org/10.1038/s41561-022-00991-6, 2022.

Clough, S. A., et al.: Atmospheric Radiative Transfer Modeling: A Summary of the AER Codes. *J. Quant. Spectrosc. Radiat. Transf.*, *91*(2), 233–244. https://doi.org/10.1016/j.jqsrt. 2004.05.058, 2005.

Dagan, G., et al.: Time-dependent, non-monotonic response of warm convective cloud fields to changes in aerosol loading. *Atmospheric Chemistry and Physics*, *17*(12), 7435–7444. https://doi.org/10.5194/acp-17-7435-2017, 2017.

Diamond, M. S., et al.: Substantial Cloud Brightening From Shipping in Subtropical Low Clouds. *AGU Adv.*, *1*(1), 1–28. https://doi.org/10.1029/2019av000111, 2020.

Feingold, G., Goren, T., and Yamaguchi, T.: Quantifying Albedo Susceptibility Biases in Shallow Clouds. *Atmos. Chem. Phys.*, 3303–3319. https://doi.org/10.5194/acp-2021-859, 2021.

Forster, P., et al.: The Earth's Energy Budget, Climate Feedbacks, and Climate Sensitivity. In Climate Change 2021: The Physical Science Basis. Contribution of Working Group I to the Sixth Assessment Report of the Intergovernmental Panel on Climate Change [Masson-Delmotte, V., P. Zhai, A. Pirani, S.L. Connors, C. Péan, S. Berger, N. Caud, Y. Chen, L. Goldfarb, M.I. Gomis, M. Huang, K. Leitzell, E. Lonnoy, J.B.R. Matthews, T.K. Maycock, T. Waterfield, O. Yelekçi, R. Yu, and B. Zhou (eds.)]. Cambridge University Press, Cambridge, United Kingdom and New York, NY, USA, pp. 923–1054, doi:10.1017/9781009157896.009, 2021.

Gelaro, R., et al.: The Modern-Era Retrospective Analysis for Research and Applications, version 2 (MERRA-2). *J. Clim.*, *30*(14), 5419–5454. https://doi.org/10.1175/JCLI-D-16-0758.1, 2017.

Ghan, S., et al.: Challenges in Constraining Anthropogenic Aerosol Effects on Cloud Radiative Forcing using Present-Day Spatiotemporal Variability. *Proc. Natl. Acad. Sci. U.S.A.*, *113*(21), 5804–5811. https://doi.org/10.1073/pnas.1514036113, 2016.

Glassmeier, F., et al.: Aerosol-Cloud-Climate Cooling Overestimated by Ship-Track Data. *Science*, *371*(6528), 485–489. https://doi.org/10.1126/science.abd3980, 2021.

505 Goren, T., et al.: Projecting Stratocumulus Transitions on the Albedo — Cloud Fraction Relationship Reveals Linearity of Albedo to Droplet Concentrations. *Geophys. Res. Lett.*, https://doi.org/10.1029/2022GL101169, 2022.

Grosvenor, D. P., et al.: Remote Sensing of Droplet Number Concentration in Warm Clouds: A Review of the Current State of Knowledge and Perspectives. *Rev. Geophy.*, 56(2), 409–453. https://doi.org/10.1029/2017RG000593, 2018.

Gryspeerdt, E., Quaas, J., and Bellouin, N.: Constraining the Aerosol Influence on Cloud Fraction. *J. Geophys. Res. Atmos.*,
510 121(7), 3566–3583. https://doi.org/10.1002/2015JD023744, 2016.

Gryspeerdt, E., et al.: Constraining the Aerosol Influence on Cloud Liquid Water Path. *Atmos. Chem. Phys.*, 19(8), 5331–5347. https://doi.org/10.5194/acp-19-5331-2019, 2019.

Gryspeerdt, E., et al.: Surprising Similarities in Model and Observational Aerosol Radiative Forcing Estimates. *Atmos. Chem. Phys.*, 20(1), 613–623. https://doi.org/10.5194/acp-20-613-2020, 2020.

515 Gryspeerdt, E., et al.: The Impact of Sampling Strategy on the Cloud Droplet Number Concentration Estimated from Satellite Data. *Atmos. Meas. Tech.*, 15(12), 3875–3892. https://doi.org/10.5194/amt-15-3875-2022, 2022.

IPCC, Annex III: Tables of historical and projected well-mixed greenhouse gas mixing ratios and effective radiative forcing of all climate forcers [Dentener F.J., B. Hall, C. Smith (eds.)]. In Climate Change 2021: The Physical Science Basis. Contribution of Working Group I to the Sixth Assessment Report of the Intergovernmental Panel on Climate Change
520 [Masson-Delmotte, V., P. Zhai, A. Pirani, S.L. Connors, C. Péan, S. Berger, N. Caud, Y. Chen, L. Goldfarb, M.I. Gomis, M. Huang, K. Leitzell, E. Lonnoy, J.B.R. Matthews, T.K. Maycock, T. Waterfield, O. Yelekçi, R. Yu, and B. Zhou (eds.)]. Cambridge University Press, Cambridge, United Kingdom and New York, NY, USA, pp. 2139–2152, doi:10.1017/9781009157896.017, 2021.

Jia, H., et al.: Significant Underestimation of Radiative Forcing by Aerosol–Cloud Interactions Derived from Satellite-Based
525 Methods. *Nat. Commun.*, 12(1), 1–11. https://doi.org/10.1038/s41467-021-23888-1, 2021.

Kang, L., et al.: Coalescence Scavenging Drives Droplet Number Concentration in Southern Ocean Low Clouds. *Geophys. Res. Lett.*, 49(7), 1–10. https://doi.org/10.1029/2022GL097819, 2022.

Kinne, S.: Aerosol radiative effects with MACv2. *Atmos. Chem. Phys.*, 19(16), 10919–10959. https://doi.org/10.5194/acp-19-10919-2019, 2019.

530 Loeb, N. G., et al.: Clouds and the Earth's Radiant Energy System (CERES) Energy Balanced and Filled (EBAF) Top-of-Atmosphere (TOA) Edition-4.0 Data Product. *J. Clim.*, 31(2), 895–918. https://doi.org/10.1175/JCLI-D-17-0208.1, 2018.

Ma, P., et al.: Observational Constraint on Cloud Susceptibility Weakened by Aerosol Retrieval Limitations. *Nat. Commun.*, 9(1), 1–10. https://doi.org/10.1038/s41467-018-05028-4, 2018.

Matthews, H. D., and Zickfeld, K.: Climate Response to Zeroed Emissions of Greenhouse Gases and Aerosols. *Nat. Clim. Change*, 2(5), 338–341. https://doi.org/10.1038/nclimate1424, 2012.
535

Mauger, G. S., and Norris, J. R.: Meteorological Bias in Satellite Estimates of Aerosol-Cloud Relationships. *Geophys. Res. Lett.*, 34(16), 1–5. https://doi.org/10.1029/2007GL029952, 2007.

Mauritsen, T., and Pincus, R.: Committed Warming Inferred from Observations. *Nat. Clim. Change*, *7*(9), 652–655. https://doi.org/10.1038/nclimate3357, 2017.

540 Myers, T. A., et al.: Observational Constraints on Low Cloud Feedback Reduce Uncertainty of Climate Sensitivity. *Nat. Clim. Change*, *11*(6), 501–507. https://doi.org/10.1038/s41558-021-01039-0, 2021.

Painemal, D., et al.: Aerosol and Cloud Microphysics Covariability in the Northeast Pacific Boundary Layer Estimated with Ship-Based and Satellite Remote Sensing Observations. *J. Geophys. Res. Atmos.*, *122*(4), 2403–2418. https://doi.org/10.1002/2016JD025771, 2017.

545 Painemal, D., and Zuidema, P.: Assessment of MODIS Cloud Effective Radius and Optical Thickness Retrievals over the Southeast Pacific with VOCALS-REx In Situ Measurements. *J. Geophys. Res. Atmos.*, *116*(24), 1–16. https://doi.org/10.1029/2011JD016155, 2011.

Pincus, R., and Baker, M. B.: Effect of Precipitation on the Albedo Susceptibility of Clouds in the Marine Boundary Layer. *Nature*, *372*(6503), 250–252. https://doi.org/10.1038/372250a0, 1994.

550 Pincus, R., et al.: Updated observations of clouds by MODIS for global model assessment, *Earth Syst. Sci. Data*, 15, 2483–2497, https://doi.org/10.5194/essd-15-2483-2023, 2023.

Platnick, S.: Vertical Photon Transport in Cloud Remote Sensing Problems. *J. Geophys. Res. Atmos.*, *105*(D18), 22919–22935. https://doi.org/10.1029/2000JD900333, 2020.

Platnick, S., et al.: MODIS Atmosphere L2 Cloud Product (06_L2). NASA MODIS Adaptive Processing System, Goddard 555 Space Flight Center, USA: http://dx.doi.org/10.5067/MODIS/MYD06_L2.061, 2015.

Platnick, S., et al.: The MODIS Cloud Optical and Microphysical Products: Collection 6 Updates and Examples from Terra and Aqua. *IEEE Trans. Geosci. Remote Sens.*, *3*(2), 163–186. https://doi.org/10.1109/TGRS.2016.2610522, 2017.

Possner, A., et al.: The Efficacy of Aerosol-Cloud Radiative Perturbations from Near-Surface Emissions in Deep Open-Cell Stratocumuli. *Atmos. Chem. Phys.*, *18*(23), 17475–17488. https://doi.org/10.5194/acp-18-17475-2018, 2018.

560 Randles, C. A., et al.: The MERRA-2 Aerosol Reanalysis, 1980 Onward. Part I: System Description and Data Assimilation Evaluation. *J. Clim.*, *30*(17), 6823–6850. https://doi.org/10.1175/JCLI-D-16-0609.1, 2017.

Rosenfeld, D., Kaufman, Y. J., and Koren, I.: Switching Cloud Cover and Dynamical Regimes from Open to Closed Benard Cells in Response to the Suppression of Precipitation by Aerosols. *Atmos. Chem. Phys.*, *6*(9), 2503–2511. https://doi.org/10.5194/acp-6-2503-2006, 2006.

565 Rosenfeld, D., et al.: Aerosol-Driven Droplet Concentrations Dominate Coverage and Water of Oceanic Low-Level Clouds. *Science*, *363*(6427). https://doi.org/10.1126/science. aav0566, 2019.

Rosenfeld, D., et al.: Global Observations of Aerosol-Cloud-Precipitation-Climate Interactions. *Rev. Geophys.*, *52*, 750–808. https://doi.org/10.1002/2013RG000441, 2014.

Scott, R. C., et al.: Observed Sensitivity of Low-Cloud Radiative Effects to Meteorological Perturbations over the Global 570 Oceans. *J. Clim.*, *33*(18), 7717–7734. https://doi.org/10.1175/JCLI-D-19-1028.1, 2020.

Seifert, A., et al.: Large-Eddy Simulation of the Transient and Near-Equilibrium Behavior of Precipitating Shallow Convection. *J. Adv. Model. Earth Syst.*, *6*, 513–526. https://doi.org/10.1002/2015MS000470, 2015.

Sherwood, S. C., et al.: An Assessment of Earth's Climate Sensitivity Using Multiple Lines of Evidence. *Rev. Geophys.*, *58*(4), 1–92. https://doi.org/10.1029/2019RG000678, 2020.

575   Small, J. D., et al.: Can Aerosol Decrease Cloud Lifetime? *Geophys. Res. Lett.*, *36*(16), 1–5. https://doi.org/10.1029/2009GL038888, 2009.

Smith, C. J., et al.: Energy Budget Constraints on the Time History of Aerosol Forcing and Climate Sensitivity. *J. Geophys. Res. Atmos.*, *126*(13), 1–20. https://doi.org/10.1029/2020JD033622, 2021.

Smith, S. J., et al.: Anthropogenic Sulfur Dioxide Emissions: 1850-2005. *Atmos. Chem. Phys.*, *11*(3), 1101–1116.
580   https://doi.org/10.5194/acp-11-1101-2011, 2011.

Stevens, B.: Rethinking the Lower Bound on Aerosol Radiative Forcing. *J. Clim.*, *28*(12), 4794–4819. https://doi.org/10.1175/JCLI-D-14-00656.1, 2015.

Sun, M., et al.: Clouds and the Earth's Radiant Energy System (CERES) FluxByCldTyp Edition 4 Data Product. *J. Atmos. Ocean. Technol.*, *39*(3), 303–318. https://doi.org/10.1175/jtech-d-21-0029.1, 2022.

585   Toll, V., et al.: Weak average liquid-cloud-water response to anthropogenic aerosols. *Nature*, *572*(7767), 51–55. https://doi.org/10.1038/s41586-019-1423-9, 2019.

Twomey, S.: Influence of Pollution on Shortwave Albedo of Clouds. *J. Atmos. Sci.*, 34, 1149–1152, doi:10.1175/1520-0469(1977)034,1149:TIOPOT.2.0.CO;2, 1977.

Wall, C. J., et al.: Assessing Effective Radiative Forcing from Aerosol–Cloud Interactions over the Global Ocean. *Proc.*
590   *Natl. Acad. Sci. U.S.A.*, *119*(46). https://doi.org/10.1073/pnas. 2210481119, 2022.

Wilks, D. S.: "The Stippling Shows Statistically Significant Grid Points." How Research Results are Routinely Overstated and Overinterpreted, and What to Do about It. *Bull. Am. Meteorol. Soc.*, *97*, 2263–2274. https://doi.org/10.1175/BAMS-D-15-00267.1, 2016.

Wood, R., et al.: Precipitation Driving of Droplet Concentration Variability in Marine Low Clouds. *J. Geophys. Res. Atmos.*,
595   *117*(19), 1–11. https://doi.org/10.1029/2012JD018305, 2012.

Wood, R., and Bretherton, C. S.: On the Relationship Between Stratiform Low Cloud Cover and Lower-Tropospheric Stability. *J. Clim.*, *19*(24), 6425–6432. https://doi.org/10.1175/JCLI3988.1, 2006.

Zelinka, M. D., Klein, S. A., and Hartmann, D. L.: Computing and Partitioning Cloud Feedbacks Using Cloud Property Histograms. Part I: Cloud Radiative Kernels. *J. Clim.*, *25*(11), 3715–3735. https://doi.org/10.1175/JCLI-D-11-00248.1,
600   2012.

Zelinka, M. D., et al.: Contributions of Different Cloud Types to Feedbacks and Rapid Adjustments in CMIP5. *J. Clim.*, *26*(14), 5007–5027. https://doi.org/10.1175/JCLI-D-12-00555.1, 2013.

Zelinka, M. D., et al.: Quantifying Components of Aerosol-Cloud-Radiation Interactions in Climate Models. *J. Geophys. Res. Atmos.*, *119*(12), 7599–7615. https://doi.org/10.1002/2014JD021710, 2014.

605   Zhang, Z., and Platnick, S.: An Assessment of Differences Between Cloud Effective Particle Radius Retrievals for Marine Water Clouds from three MODIS Spectral Bands. *J. Geophys. Res. Atmos.*, *116*(20), 1–19. https://doi.org/10.1029/2011JD016216, 2011.

Zhu, Y., Rosenfeld, D., and Li, Z.: Under What Conditions Can We Trust Retrieved Cloud Drop Concentrations in Broken Marine Stratocumulus? *J. Geophys. Res. Atmos.*, *123*(16), 8754–8767. https://doi.org/10.1029/2017JD028083, 2018.
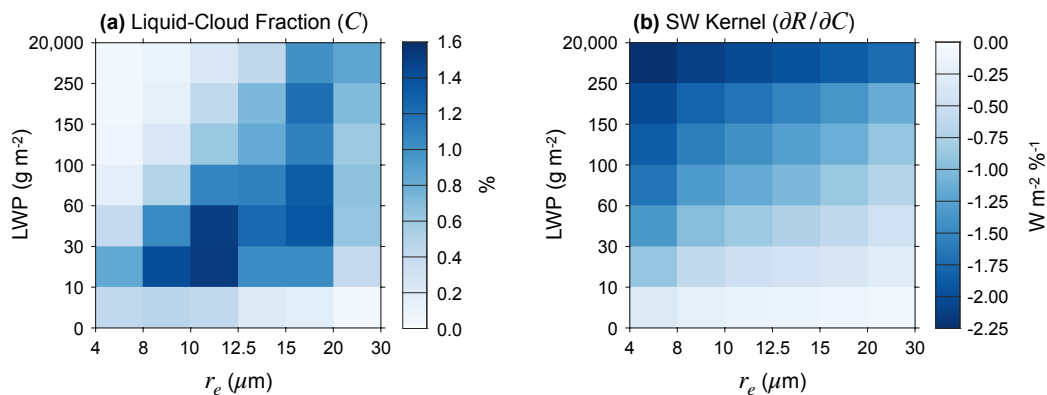
Figures

Figure 1. Annual-mean climatology of MODIS cloud observations and the SW cloud radiative kernel over ocean between 55°S and 55°N. (a) Joint histogram of liquid-cloud fraction (C) partitioned by liquid water path (LWP) and cloud-droplet effective radius (r_e). (b) SW cloud radiative kernel. The kernel represents $\partial R / \partial C$, where R is the SW radiative effect of liquid clouds at the top of the atmosphere.
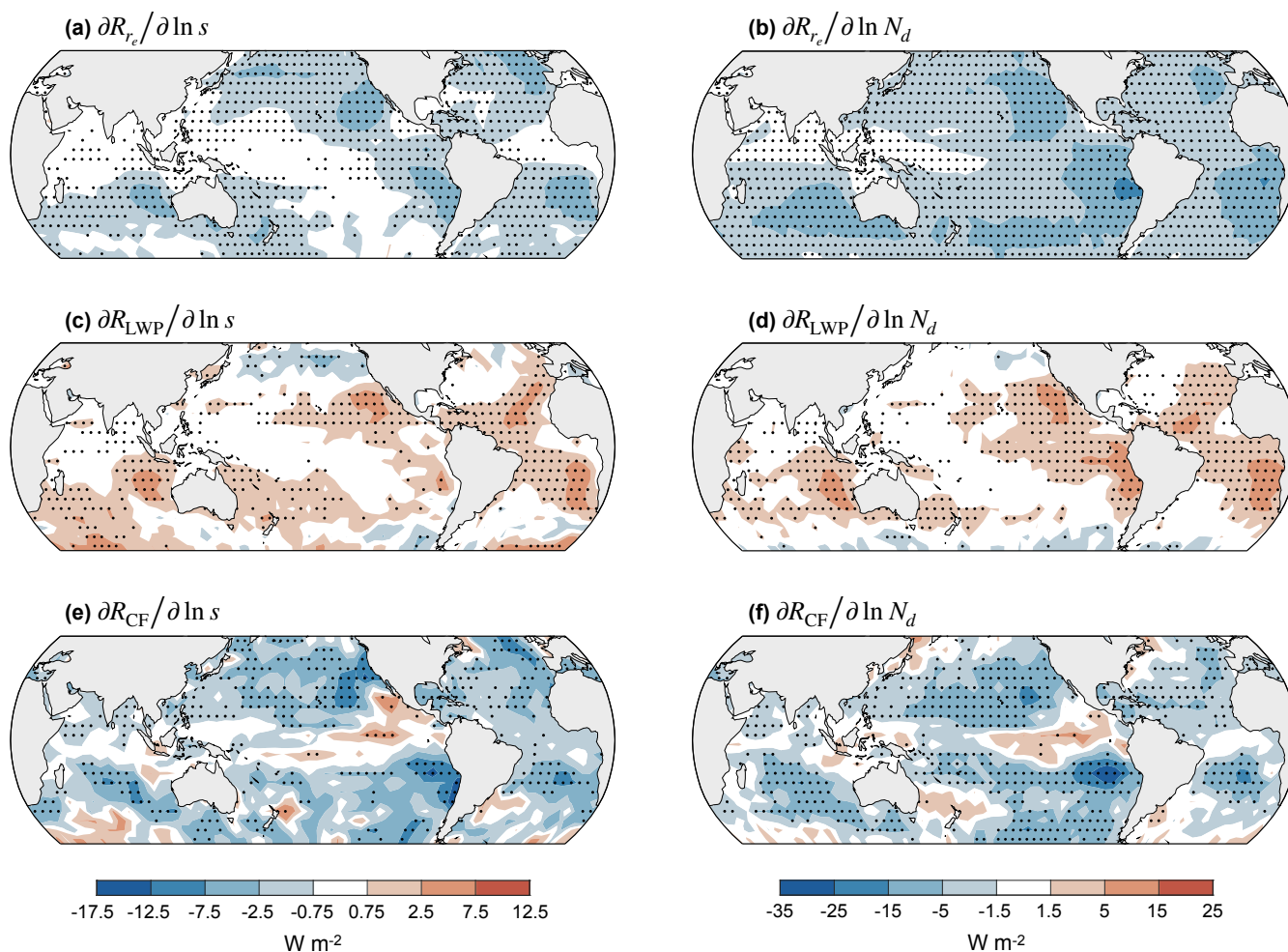
Figure 2. Aerosol indirect effects estimated with two indicators of CCN concentration: sulfate aerosol mass concentration at 910 hPa (s) and cloud droplet number concentration from pixels with the largest 10% optical thickness (N_d). Linear regression coefficients are shown for (a) $\partial R_{r_e}/\ln s$, (b) $\partial R_{r_e}/\ln N_d$, (c) $\partial R_{\mathrm{LWP}}/\ln s$, (d) $\partial R_{\mathrm{LWP}}/\ln N_d$, (e) $\partial R_{\mathrm{CF}}/\ln s$, and (f) $\partial R_{\mathrm{CF}}/\ln N_d$, where R_{r_e}, R_{LWP}, and R_{CF} are the top-of-atmosphere SW flux perturbations caused by r_e anomalies, LWP anomalies, and cloud-fraction anomalies, respectively. (a-b) represents the Twomey effect, (c-d) represents the LWP adjustment, and (e-f) represents the cloud-fraction adjustment. Stippling indicates regression coefficients that are significantly different from zero with the false discovery rate limited to 0.1 (Wilks, 2016). Cloud radiative effects are computed with only fully cloudy pixels included in the cloud histograms (MODIS$_{\mathrm{CLD}}$). Note that the contour values in (a), (c), and (e) are proportional to those in (b), (d), and (f).
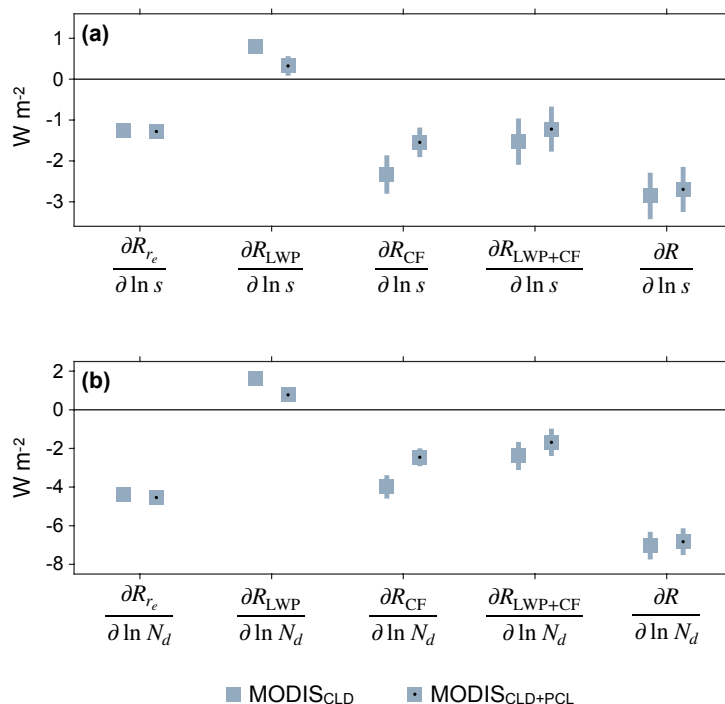
Figure 3. Spatial averages of the regression coefficients that represent aerosol indirect effects. Averages are computed over ocean between 55°S and 55°N. (a) Aerosol indirect effects estimated with s as the CCN indicator. $\partial R_{\mathrm{LWP+CF}}/\partial \ln s$ is the total cloud adjustment ($R'_{\mathrm{LWP+CF}} \equiv R'_{\mathrm{LWP}} + R'_{\mathrm{CF}}$). The MODIS$_{\mathrm{CLD}}$ case is computed with only fully cloudy pixels included in the cloud histograms, and the MODIS$_{\mathrm{CLD+PCL}}$ case is computed with both fully and partly cloudy pixels included. (b) Similar to (a), except that N_d is the CCN indicator. Squares show mean values, and vertical lines show 95% CIs.
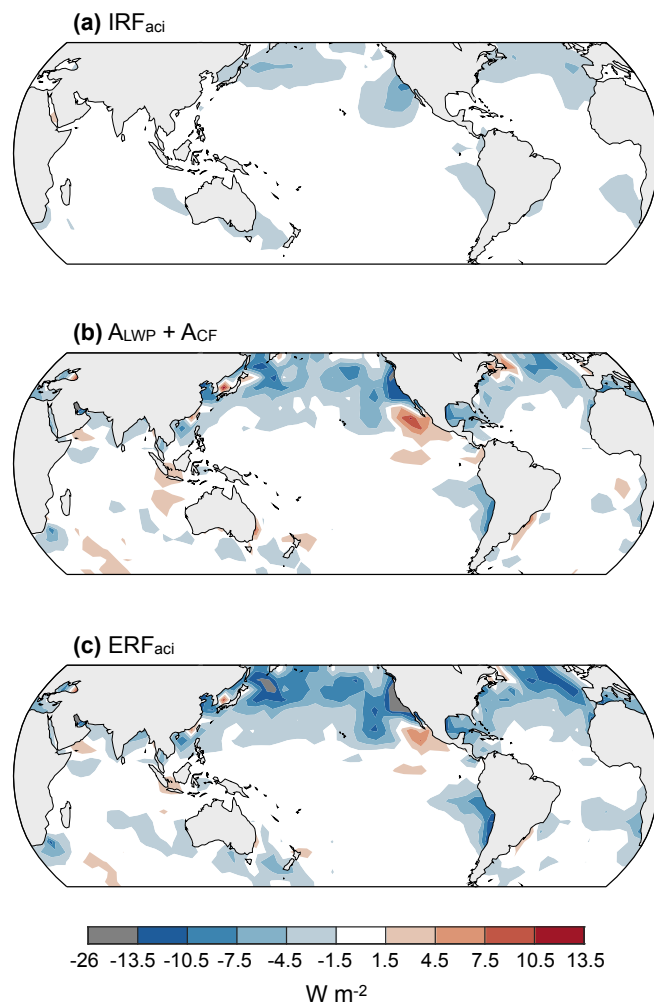
Figure 4. Components of historical ERF$_{aci}$ from liquid clouds, including (a) the Twomey effect (IRF$_{aci}$), (b) the total cloud adjustment (A$_{LWP}$ + A$_{CF}$), and (c) the overall ERF$_{aci}$. The estimates represent SW forcing, and they are computed with only fully cloudy pixels included in the cloud histograms (MODIS$_{CLD}$).
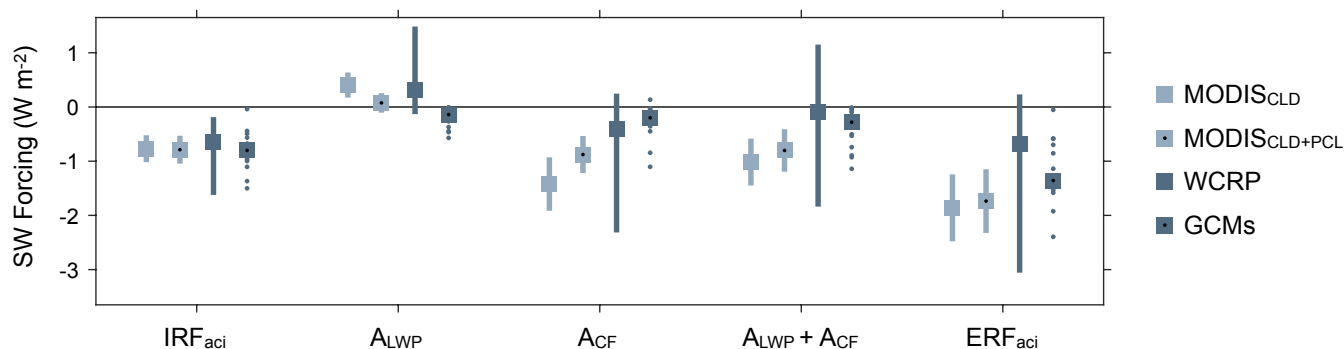
640

Figure 5. Components of SW ERF_{aci} for liquid clouds averaged over ocean between 55°S and 55°N. The "MODIS$_{CLD}$" and "MODIS$_{CLD+PCL}$" cases show estimates from this study. The "WCRP" case is computed with the method of Bellouin et al.

645 (2020). The "GCMs" case shows values from 14 CMIP5 and AeroCom models computed by Gryspeerdt et al. (2020). The WCRP and GCM estimates are modified from their original published values so that they represent averages over ocean between 55°S and 55°N. Squares show median values, vertical lines show 95% CIs, and dots in the "GCMs" case show individual models.
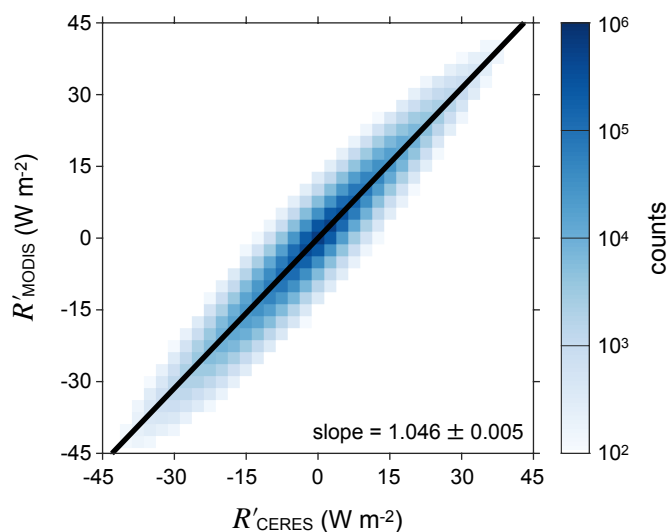
Figure A1. Validation of the SW cloud radiative kernel. The vertical axis shows monthly SW flux anomalies induced by liquid clouds estimated with the radiative kernel and MODIS r_e-LWP joint histogram (R'_{MODIS}). The horizontal axis shows monthly SW flux anomalies induced by liquid clouds observed by CERES (R'_{CERES}). Data are plotted as a joint histogram compiled from all monthly $1° \times 1°$ grid boxes over ocean between 55°S and 55°N from 2003 through 2020. The color scale is logarithmic, and bins with fewer than 100 counts are shaded white for clarity. The black line is the ordinary least-squares regression fit. The regression slope and its 95% CI are printed in the bottom right corner.
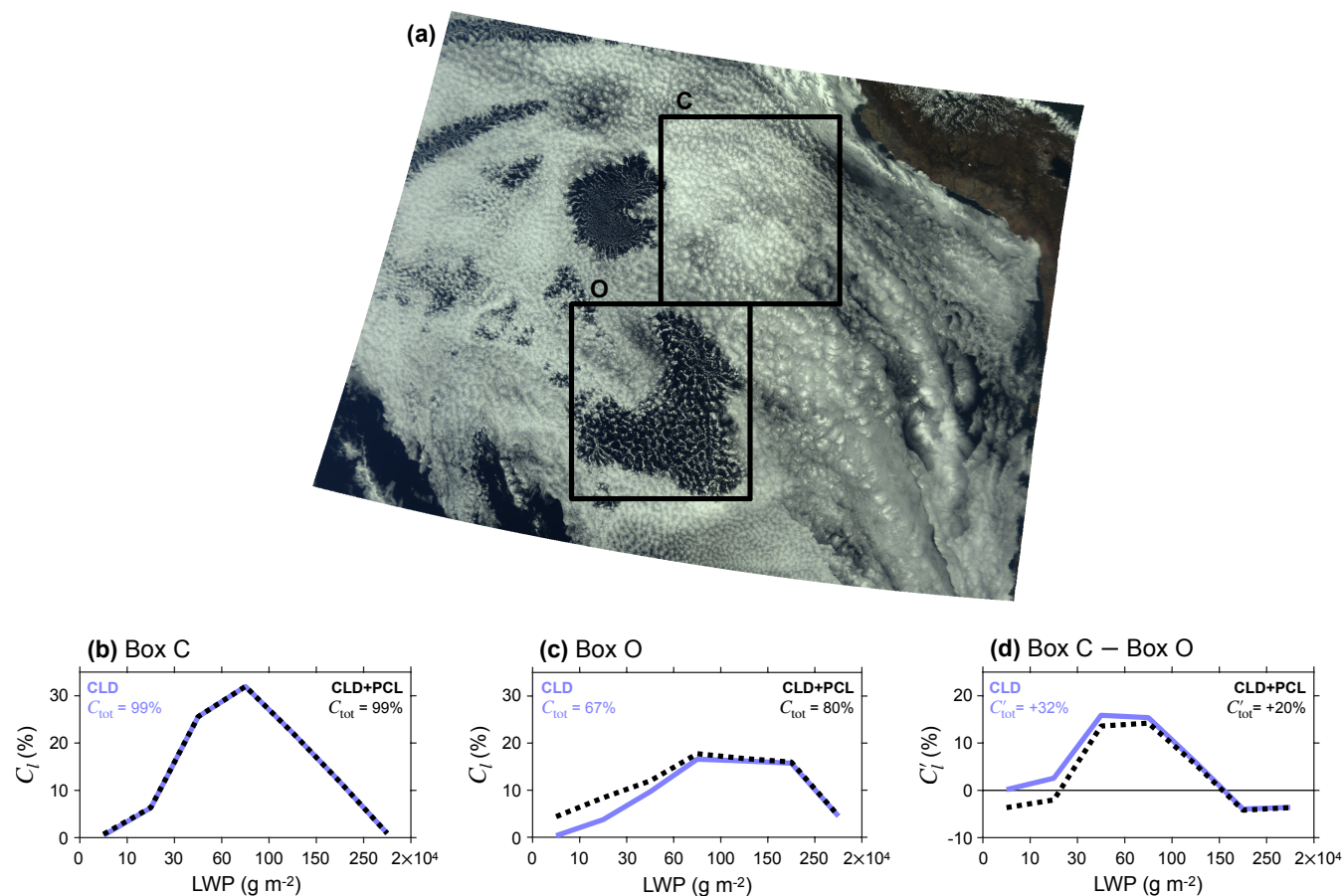
Figure D1. Case study demonstrating how different filtering methods for partly cloudy pixels lead to different estimates of LWP and cloud-fraction anomalies when the cloud morphology changes. (a) Visible image of stratocumulus clouds over the Southeast Pacific Ocean taken on September 27, 2019 from MODIS onboard the Terra satellite. Most clouds in box C exhibit closed mesoscale cellular convection, and most clouds in box O exhibit open mesoscale cellular convection. Both boxes span 6° latitude and 6° longitude. (b) Liquid-cloud fraction partitioned by LWP (C_l) in box C. In case CLD, the C_l histogram includes only fully cloudy pixels, and in case CLD+PCL, the histogram includes both fully and partly cloudy pixels. The CLD and CLD+PCL cases are shown with blue and black-dashed lines, respectively. (c-d) Similar to (b) except that (c) shows box O and (d) shows the difference between box C and box O. Primes in (d) represent the box-C average minus the box-O average.